

# High-quality Nano-patterning of Oxide Interfaces Using Transferred Gold Masks

Qing Xiao<sup>1,2</sup>, Yanling Liu<sup>1</sup>, Changjian Ma<sup>1</sup>, Danqing Liu<sup>1</sup>, Zhiyuan Qin<sup>1,3</sup>, Qianyi Zhao<sup>1</sup>, Chengyuan Huang<sup>1,2</sup>, Mengke Ha<sup>1</sup>, Zhenhao Li<sup>1</sup>, and Guanglei Cheng<sup>\*1,2,3</sup>

<sup>1</sup>Laboratory of Spin Magnetic Resonance, School of Physical Sciences, Anhui Province Key Laboratory of Scientific Instrument Development and Application, University of Science and Technology of China, Hefei 230026, China

<sup>2</sup>Hefei National Research Center for Physical Sciences at the Microscale, University of Science and Technology of China, Hefei 230026, China

<sup>3</sup>Hefei National Laboratory, University of Science and Technology of China, Hefei 230088, China

## Abstract

Complex oxide interfaces, such as SrTiO<sub>3</sub> and KTaO<sub>3</sub> based heterostructures, host rich correlated phenomena with strong potential for advanced device applications. However, these interfaces are extremely susceptible to contamination and defect formation during nanofabrication, which often compromises device performance. Here, we present a solvent-free method for patterning oxide interfaces by employing high-resolution transferable thin metal masks in conjunction with oxygen-enriched Ar<sup>+</sup> ion milling, which enables a clean and well-controlled nanofabrication process. Transport measurements demonstrate that the fabricated devices preserve their intrinsic properties, including high carrier mobilities, with negligible degradation compared to the pristine interfaces. This technique offers a convenient and robust route for engineering high-performance oxide electronic devices with precisely tailored transport characteristics.

## 1 Introduction

Oxide interfaces host a rich spectrum of emergent quantum phenomena, including two-dimensional electron gas (2DEG)<sup>1</sup>, metal-insulator transitions<sup>2</sup>, superconductivity<sup>3</sup>, and spin-orbit coupling<sup>4,5</sup>. These properties arise from delicate electronic reconstruction and various symmetry-breaking states, and are prone to environmental perturbations due to the proximity of the interface and surface. To harness these effects for functional quantum devices, precise control over nanofabrication is essential, requiring methods that minimize structural and electronic disorder while enabling high-resolution patterning.

Current nanofabrication methods for oxide heterostructures can be broadly classified into two categories: top-down material removal<sup>6-8</sup> and bottom-up selective deposition<sup>9-18</sup>. For perovskite substrates like SrTiO<sub>3</sub> (STO) and KTaO<sub>3</sub> (KTO), conventional Ar<sup>+</sup> ion etching often induces undesirable conductive channels<sup>19,20</sup>. Modified methods including low energy<sup>6</sup> or low temperature Ar<sup>+</sup> ion etching<sup>7</sup> and BCl<sub>3</sub>-based reactive ion etching<sup>8</sup> have been explored to mitigate such parasitic conduction. Alternatively, selective wet etching has proven potential for certain oxides<sup>21</sup>. In bottom-up approaches, oxides are epitaxially selectively deposited with predefined masks. Conventional polymer masks decompose at elevated temperatures, restricting their use to room-temperature depositions<sup>18</sup>. High-temperature compatible hard masks are widely used instead<sup>9-17</sup>. However, these conventional approaches inevitably expose the critical interfaces or surfaces

---

\*Email: glcheng@ustc.edu.cn

to polymer residues or chemical solutions, potentially inducing detrimental modifications to the interfacial electronic structure through unintended doping<sup>22,23</sup>, defect formation, or surface redox reactions<sup>24</sup>. While silicon stencil masks<sup>25</sup> can mitigate contamination, the fragility, complex fabrication process, relatively large size and edge blurring effect limit their applicability for complex device architectures.

Reconfigurable patterning has been realized in some oxide interfaces like  $\text{LaAlO}_3/\text{SrTiO}_3$  (LAO/STO) and  $\text{LaAlO}_3/\text{KTaO}_3$  (LAO/KTO) via conductive atomic force microscopy (cAFM)<sup>26</sup> and focused electron beam irradiation<sup>27</sup>, which control insulator-metal transitions locally and reversibly at extreme resolutions. Nanoscale structures created with high precision have exhibited exceptional quantum transport properties<sup>28–30</sup>. However, the stability of devices remains fundamentally limited by degradation in ambient conditions<sup>31</sup>.

In this work, we present an advanced nanofabrication technique utilizing transferable Au films as hard masks in combination with oxygen-enriched  $\text{Ar}^+$  ion milling. The method successfully preserves the high-mobility characteristics of oxide interfaces after nanofabrication. Significantly, the fabricated devices achieved a feature size  $\sim 100$  nm, limited by the resolution of the Au masks we used. In addition, our methodology demonstrates full compatibility with both top-down and bottom-up fabrication approaches, providing a versatile platform for quantum engineering in oxides.

## 2 Results and Discussion

To eliminate residue during patterning, we developed a contamination-free patterning technique based on transferable Au films as hard masks and oxygen-enriched  $\text{Ar}^+$  ion milling. Figure 1 and S1 illustrate the implementation of this method in the top-down approach. Prior to oxide patterning, Au masks were prepared by first depositing a 5–10 nm Au layer on the whole surface of clean  $\text{SiO}_2/\text{Si}$  substrates, and followed by depositing 80–100 nm Au film in patterns defined by ultraviolet lithography (UVL) or electron-beam lithography (EBL). Then we use a dome-shaped polymer stamp (NOA 81, Norland optical adhesive) to pick up a thick Au pattern as well as the thin Au layer within the stamp’s contact area (see Figure 1a, 1b) at 55 °C. Subsequently, the Au pattern is released on LAO/STO at 150 °C, with the thin Au layer outside the patterned area remaining on the stamp (Figure 1c, 1d, S2). Notably, this is a completely dry transfer process that eliminates the need for polymer melting or solvent immersion, as well as contact between the polymer and the rest of the sample, thanks to the Au isolation layer (Supporting Movies SM1, SM2). Next,  $\text{Ar}^+$  ion milling is performed in an  $\text{Ar}/\text{O}_2$  gas mixture at a ratio of 1:5 (Figure 1e). Finally, the Au mask is removed by another stamp at room temperature, yielding a patterned LAO/STO Hall bar (Figure 1f).

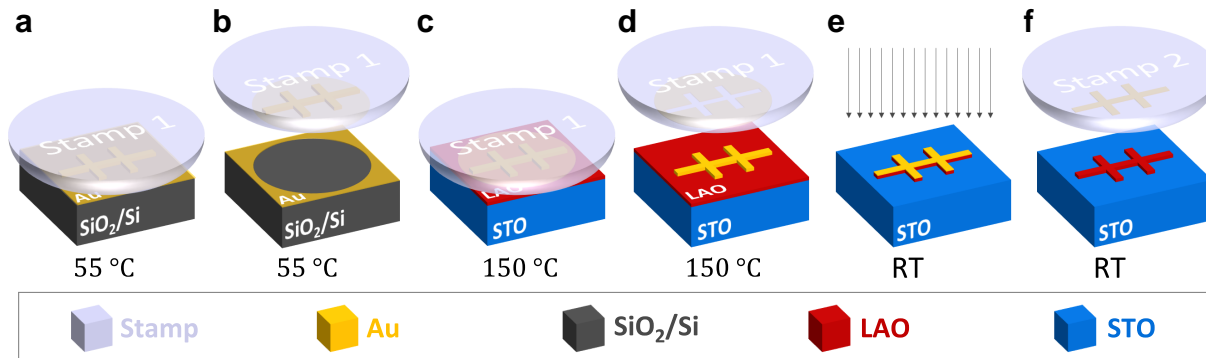


Figure 1: Illustration of an Au Hall bar mask transfer in the top-down patterning approach. (a,b) A stamp is used to pick up a pre-patterned Au Hall bar mask with the thin Au layer on  $\text{SiO}_2/\text{Si}$ . (c,d) The Au Hall bar, along with the thin Au layer directly beneath it, is released on the LAO/STO sample. The thin Au layer outside the patterned area remains adhered to the stamp, thereby preventing direct contact between the stamp and the sample. (e) Oxygen-enriched  $\text{Ar}^+$  ion milling removes the exposed LAO. (f) A second stamp is used to pick up the Au mask on the LAO/STO.

In the fabrication of 2D material transistors and flexible electronics, multiple methods have been developed to achieve dry transfer printing of metal electrodes<sup>32–43</sup> and complex ultrathin films<sup>44–46</sup> on arbitrary substrates. However, these approaches exhibit limitations in patterning sensitive oxide interfaces, partially due to residues from the polymer stamps, e.g., poly(methyl methacrylate) (PMMA)<sup>32,33,35,38–43,45,46</sup>, polymer polypropylene carbonate (PPC)<sup>34</sup>, polyvinyl alcohol (PVA)<sup>37,46</sup> or polystyrene (PS)/poly(4-vinyl pyridine) (P4VP)<sup>44</sup>. Further immersion in acetone, chloroform, water or other solvents is necessary to remove the residues. In addition, these methods typically require a pre-functionalization layer such as hexamethyldisilazane (HMDS)<sup>32–34,39</sup>, octadecyltrichlorosilane (OTS)<sup>45</sup> or a sacrificial graphene interlayer<sup>37,38,41</sup> to reduce strong adhesion to silicon substrates, which complicates the experimental workflow and risks introducing additional contaminants to oxide surfaces. Here, we employ NOA 81 as the stamp material, which is optically clean and nearly residue-free. The stamp is prepared by depositing a droplet onto a glass slide to form a dome structure, followed by UV curing (see Supporting Information SI). This method enables efficient transfer of prefabricated Au patterns from SiO<sub>2</sub>/Si substrates to target samples. Remarkably, the whole transfer process takes less than 10 min, including the curing of the stamp.

Under the specified transfer condition, Au films spanning 5–100 nm thicknesses can be consistently picked up by the polymer stamp. Notably, the success rate of releasing exhibits strong thickness dependence, with thicker films showing significantly higher release rates than thinner films. We attribute this behavior to the mechanical fragility of thin films: their tendency to form structural imperfections (e.g., wrinkles, microcracks) under stamp-induced deformation stress<sup>47,48</sup> could substantially reduce interfacial adhesion to target substrates (Figure S3).

Conventional dry transfer printing strategies typically aim for damage-free transfer by minimizing in-plane stress to prevent film fracture<sup>49</sup>. In contrast, our method deliberately leverages this inherent mechanical fragility. We exploit the strong thickness-dependent stability: thin (5–10 nm) Au layers are prone to wrinkling and cracking, while thick (80–100 nm) Au films remain robust under the same condition. This differential behavior enables a selective transfer process. The thin Au layer outside the patterned area remains adhered to the stamp, acting as an isolation layer to protect the oxide surface from direct contact with the polymer stamp. Crucially, the thin Au layer beneath the thick pattern is picked up together, forming a cohesive bilayer that is released successfully. This design effectively prevents the transfer of any contaminant from the stamp to the sample in the release step at elevated temperatures (see Figure S4), while simultaneously maintaining transfer success rates of greater than 90% for thick Au films. Thus, by strategically controlling the location of interfacial adhesion failure, we achieve residue-free patterning—transforming a common failure mode into an enabling feature of the fabrication process.

It is well-known that Ar<sup>+</sup> ion bombardment can easily create oxygen vacancies in STO and induce metallicity<sup>19</sup>. To suppress the formation of oxygen vacancies, we explored Ar<sup>+</sup> ion milling under oxygen-rich conditions. We found that an Ar/O<sub>2</sub> gas mixture ratio of 1:5 effectively etches STO without the formation of conductive channels that shunt devices. By varying the chamber pressure and bias voltage, different etch rates can be achieved. For samples in this work, the etch rate is about 2 nm/s for LAO or STO and 4–5 nm/s for transferred Au films.

Figure 2a presents an optical micrograph of a transferred Au Hall bar structure (20 μm × 5 μm) with 8 electrodes on a (3+8) uc LAO/STO sample<sup>50</sup> (Supporting Movie SM1). The final device after mask removal is shown in Figure 2b. By scratching the Au film with a tungsten tip at the corners and controlling the stamp’s contact area, a fraction of the mask is intentionally kept to serve as visual markers for wire bonding. This enables the subsequent precise bonding of aluminum wires to make ohmic contacts to the interface. The AFM topography image on the main channel of the Hall bar indicates successful pattern transfer (Figure 2c). Atomic terraces of the LAO/STO sample are clearly resolved (Figure 2d), suggesting the pristine surface is preserved during this clean transfer process. Furthermore, optimized ion milling yields well-defined edges with a sharp transition between the device and the etched region (Figure 2e). Systematic AFM characterization performed on dozens of fabricated LAO/STO devices confirms the residue-free nature of our fabrication process. The absence of any observable contamination is consistently observed, as exemplified by the topography across both the device channel and the etched region in the representative device shown in Figures 2c and 2e.

To demonstrate that the pristine interface is preserved electronically, we conducted a comparative transport study of devices fabricated with silicon mask, transferred Au mask, and UVL methods. Initially, a 1 mm × 1 mm square defined by a silicon stencil mask and a 200 μm × 200 μm square defined by a transferred

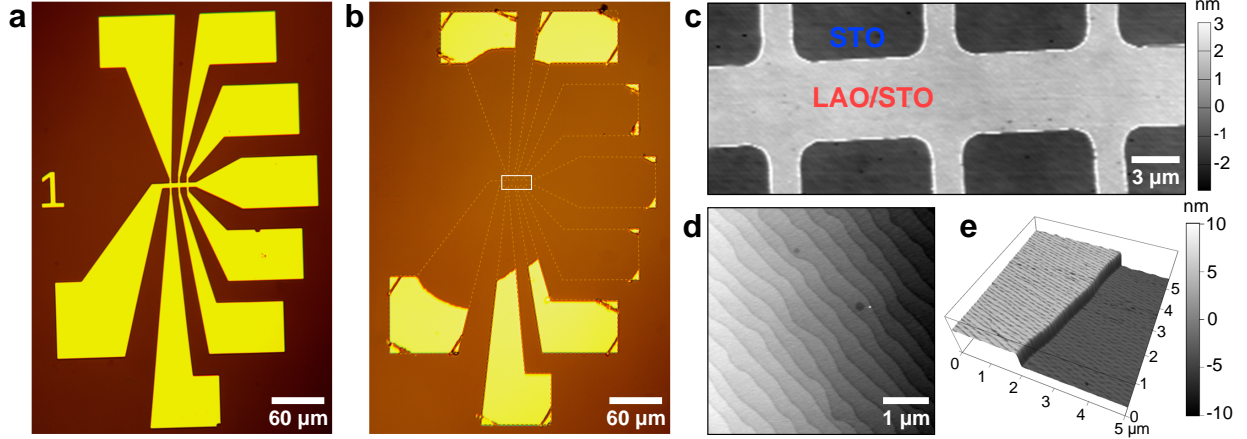


Figure 2: A Hall bar fabricated using a transferred Au mask in the top-down approach. (a) The transferred Au Hall bar pattern on LAO/STO. (b) The final LAO/STO Hall bar device. (c) AFM topography image of area highlighted within the white rectangle in (b). (d) AFM topography image of the surface of the Hall bar, preserving the atomic terraces of the pristine LAO/STO sample. (e) The abrupt edge between the device and the etched region.

Au mask were fabricated on the same  $5\text{ mm} \times 5\text{ mm}$  high mobility (3+2) uc LAO/STO sample (Sample A). After fast van der Pauw (vdP) measurement<sup>50</sup> at cryogenic temperature, UVL was employed to pattern a  $200\text{ }\mu\text{m} \times 200\text{ }\mu\text{m}$  square within the silicon-masked region. Meanwhile, the area fabricated by the Au mask method was only subjected to photoresist (PR) coating and removal during the same process. Finally, vdP measurements were performed on both regions again. As shown in Figure 3, the temperature-dependent characteristics of mobility and carrier density of the Au-masked square closely resemble those of the silicon-masked square, with very high mobilities exceeding  $10000\text{ cm}^2/\text{Vs}$  at 2 K. In contrast, the sheet resistances and carrier densities are significantly higher in the devices subjected to PR processing, suggesting more carriers are created due to the formation of oxygen vacancies. Indeed, the measured mobilities dropped to  $\sim 5000\text{ cm}^2/\text{Vs}$ , suggesting severe degradation of the interfaces. The direct comparison between pre- and post-UVL process of the Au-masked region conclusively demonstrates that the conventional UVL process causes interface deterioration, ruling out the possibility of regional inhomogeneity. To exclude potential temporal degradation, we have conducted repeated measurements over several days before UVL, confirming the stability of the interface properties.

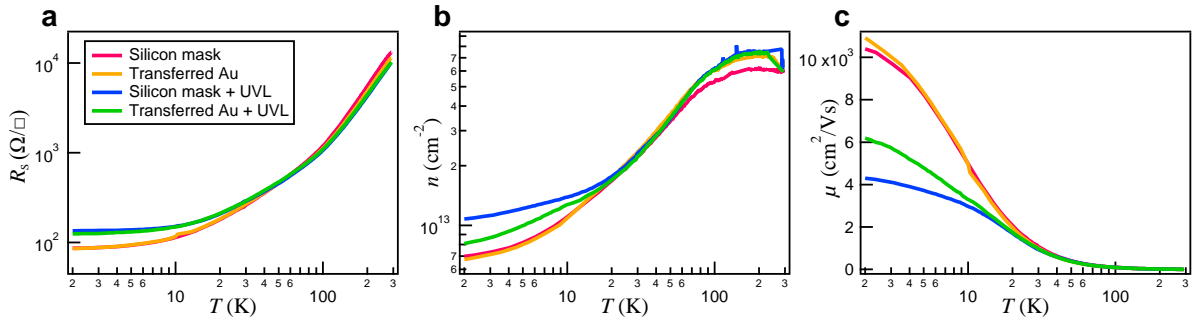


Figure 3: Temperature-dependent transport properties of patterned squares on Sample A: (a) sheet resistance  $R_s$ , (b) carrier density  $n$ , and (c) mobility  $\mu$  as functions of temperature extracted from vdP measurement.

Notably, our method successfully extends to nanoscale device fabrication through a two-step transfer

process. We first transferred a nanoscale Au Hall bar defined by EBL and then transferred UVL-patterned Au contact pads. The Au pads were carefully aligned under a microscope and laminated onto the first layer with controlled overlap (Figure 4a and Supporting Movie SM3). Figure 4b shows a  $1.6\ \mu\text{m} \times 0.4\ \mu\text{m}$  LAO/STO Hall bar structure with four 200 nm wide voltage leads. Note that the atomic terraces are well-preserved across the entire device, including the insulating regions. Figure 4c shows a functional 100 nm wide LAO/STO nanoconstriction. A clearly resolved terrace ( $\sim 0.4\ \text{nm}$ ) crossing the channel demonstrates the preservation of the original surface by the Au mask (Figure 4d). It is noteworthy that channels narrower than 500 nm exhibit increased susceptibility to deformation and cracking during transfer, thus requiring the use of flatter stamps, thicker Au and smaller contact areas to minimize mechanical strain. With this careful parameter optimization, our method proves to be robust and reproducible, as demonstrated by the consistent results across multiple transfers of patterns with nanoscale features (Supporting Movie SM 4). In contrast, the photoresist in the conventional EBL process exhibits poor resistance to oxygen-enriched  $\text{Ar}^+$  ion milling, consequently resulting in failed pattern transfer.

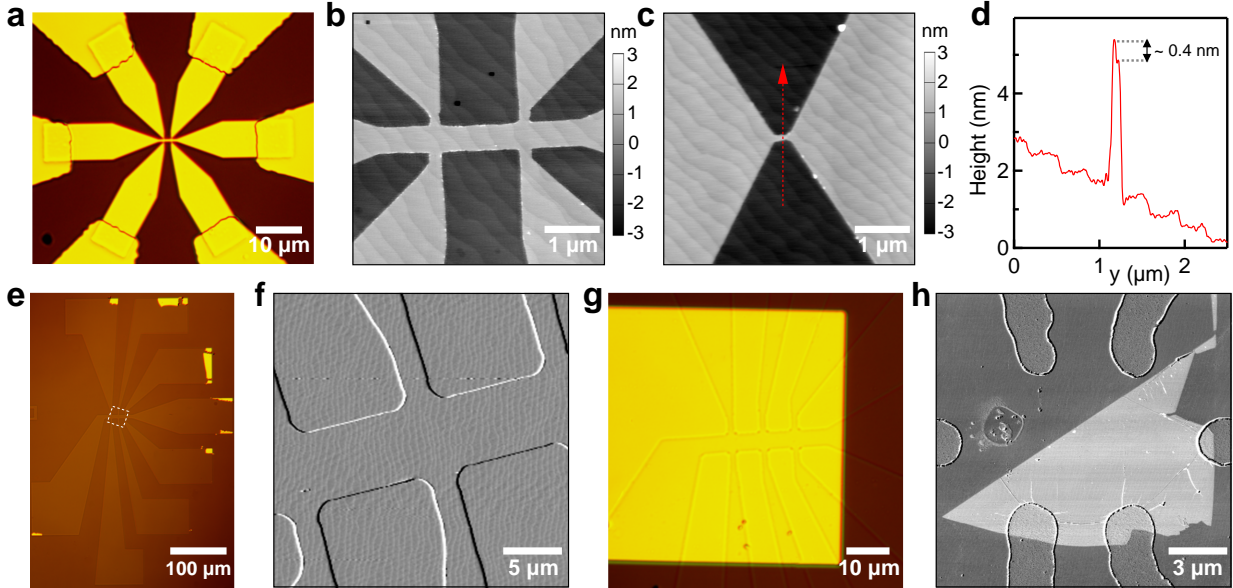


Figure 4: Versatile device fabrication. (a) The two-step-transferred nanoscale Au Hall bar pattern. (b) The final LAO/STO Hall bar device. (c) An LAO/STO nanoconstriction with a width  $\sim 100\ \text{nm}$ . (d) The height profile along the red dashed line in (c). (e) A Hall bar fabricated via the bottom-up approach. (f) AFM topography image of the area highlighted within the white dashed square in (e). (g) A Hall bar device with an Au top gate. (h) A graphene monolayer transferred onto a STO substrate with pre-patterned electrodes.

The technique of transferring Au masks can be adapted to the bottom-up approach (Figure S6). Figure 4e,f show a Hall bar fabricated by selectively depositing LAO on STO. The fabrication began with transferring a predefined Au Hall bar pattern onto the STO substrate, followed by etching the exposed regions to a depth of 10 nm. To avoid the formation of electron gas outside the Hall bar region, we deposited a 10 nm  $\text{SiO}_2$  layer. Subsequently, the Au pattern with  $\text{SiO}_2$  covered was picked up to expose only the designated Hall bar region. The final conductive Hall bar was then formed through controlled deposition of several LAO unit cells using pulsed laser deposition (PLD). Apart from patterning, this technique offers significant advantages for device integration by enabling direct transfer of top gates onto pre-fabricated structures without any additional lithography steps. This capability is illustrated in Figure 4g, which shows a Hall bar device covered by a rectangular Au top gate electrode. Furthermore, two-dimensional materials can also be transferred directly with this stamp (Figure 4h).

It is noteworthy that, two-dimensional materials such as graphene<sup>51</sup> and  $\text{CrOCl}$ <sup>52</sup> have recently been explored as masks for lithography, leveraging their etch selectivity at specific etching conditions. Similarly, while both strategies employ transferred thin films as masks to protect the underlying surface, our

approach using Au films provides a more versatile and scalable platform. Compared to the exfoliation and pre-patterning of two-dimensional materials, Au masks allow for standard fabrication via conventional lithography and evaporation, offering higher design freedom and significantly lower process complexity. This suggests the significant potential of Au masks for the future high-throughput fabrication of sensitive oxide electronic devices, while consistently maintaining a high level of quality.

### 3 Conclusion

In summary, we have developed a versatile patterning method based on transferred Au masks and oxygen-enriched Ar<sup>+</sup> ion milling. The residue-free transfer process, coupled with the protection of Au layers, effectively preserves the pristine quality of the oxide interfaces by circumventing the chemical and polymeric contamination inherent in conventional methods. This approach provides a powerful platform for probing intrinsic properties of as-grown interfaces at the nanoscale, offering new insights into the conductive behaviors and complex electron correlations at oxide heterostructures. Furthermore, the method demonstrates broad applicability beyond interface studies, including lithography-free gate integration and dry transfer of two-dimensional materials.

## 4 Experimental Section

### 4.1 Au Mask Fabrication

The transferable Au masks are fabricated through the following procedure. First, the 5–10 nm thin Au film is deposited on a clean SiO<sub>2</sub>(300 nm)/Si substrate via electron-beam evaporation at a rate of 0.5–0.8 Å/s. Subsequently, the 80–100 nm thick Au patterns for transfer are fabricated on this Au-coated substrate. The patterns are defined by either UVL or EBL, followed by Au deposition via electron-beam evaporation at a rate of 1–2 Å/s.

### 4.2 Stamp Preparation

The polymer stamp is prepared using the optical adhesive NOA 81. A droplet of NOA 81 is deposited onto a clean glass slide to form a dome-shaped structure with a diameter of approximately 3 mm. The adhesive is then cured for 3 min under a 365 nm ultraviolet lamp with a power density of 1 V/cm<sup>2</sup>, resulting in a solid, optically transparent stamp ready for the dry transfer process.

### 4.3 Au Mask Transfer

The transfer procedure for thick Au patterns fabricated on both pristine and Au-coated SiO<sub>2</sub>/Si substrates is identical. The glass slide bearing the cured polymer stamp is inverted and mounted onto a micromanipulator. Separately, the SiO<sub>2</sub>/Si substrate with the pre-fabricated Au patterns is fixed to another micromanipulator stage and positioned directly beneath the stamp. The stage holding the substrate is first heated to 55 °C. The stamp is then lowered until it makes full contact with the target Au pattern. After maintaining contact for 2 min, the stamp is lifted rapidly, picking up the Au pattern. Subsequently, the target oxide sample (e.g., LAO/STO) is placed on the heating stage beneath the stamp. The stage temperature is raised to 150 °C. The stamp, now carrying the Au pattern, is carefully lowered until the pattern makes complete contact with the oxide surface. After 30–60 s, the stamp is lifted slowly, releasing the thick Au pattern onto the target surface.

### 4.4 Oxygen-enriched Ar<sup>+</sup> Ion Milling

The oxygen-enriched Ar<sup>+</sup> ion milling is performed using either a custom-built ion milling system or a commercial system (Oxford PlasmaPro NGP80). When using the Oxford PlasmaPro NGP80, the etching is conducted with a gas flow of 10 sccm Ar and 50 sccm O<sub>2</sub>, at a radio-frequency (RF) power of 150 W. The chamber pressure varies between 20 mTorr and 50 mTorr, resulting in different etch rates.

## Acknowledgements

This work was supported by the National Key Research and Development Program of China (2024YFA1409500) and the CAS Project for Young Scientists in Basic Research (YSBR-100). This work was partially carried out at the USTC Center for Micro and Nanoscale Research and Fabrication.

## Supporting Information

- Front-view schematic of the fabrication process in Figure 1 (Figure S1); stamps after the transfer process (Figure S2); thickness-dependent Au pattern transfer behavior (Figure S3); AFM characterization of the oxide surface before and after the Au mask transfer process (Figure S4); temperature-dependent transport properties of patterned squares on a low-mobility LAO/STO sample (Figure S5); comparison of the bottom-up and the top-down patterning approaches (Figure S6). (PDF)
- Movie SM1: Transfer process of the Au Hall bar in Figure 2a. (MP4)
- Movie SM2: Transfer process of a 6-pad Au Hall bar. (MP4)
- Movie SM3: Transfer process of the contact pads in Figure 4a. (MP4)
- Movie SM4: Sequential successful transfers of multiple EBL-defined nanoscale patterns. (MP4)

## References

- [1] Ohtomo, A.; Hwang, H. A high-mobility electron gas at the LaAlO<sub>3</sub>/SrTiO<sub>3</sub> heterointerface. *Nature* **2004**, *427*, 423–426.
- [2] Thiel, S.; Hammerl, G.; Schmehl, A.; Schneider, C. W.; Mannhart, J. Tunable quasi-two-dimensional electron gases in oxide heterostructures. *Science* **2006**, *313*, 1942–1945.
- [3] Reyren, N.; Thiel, S.; Caviglia, A. D.; Kourkoutis, L. F.; Hammerl, G.; Richter, C.; Schneider, C. W.; Kopp, T.; Rüetschi, A.-S.; Jaccard, D.; Gabay, M.; Müller, D. A.; Triscone, J.-M.; Mannhart, J. Superconducting interfaces between insulating oxides. *Science* **2007**, *317*, 1196–1199.
- [4] Ben Shalom, M.; Sachs, M.; Rakhmilevitch, D.; Palevski, A.; Dagan, Y. Tuning Spin-Orbit Coupling and Superconductivity at the SrTiO<sub>3</sub>/LaAlO<sub>3</sub> Interface: A Magnetotransport Study. *Physical review letters* **2010**, *104*, 126802.
- [5] Caviglia, A.; Gabay, M.; Gariglio, S.; Reyren, N.; Cancellieri, C.; Triscone, J.-M. Tunable Rashba spin-orbit interaction at oxide interfaces. *Physical review letters* **2010**, *104*, 126803.
- [6] Paolo Aurino, P.; Kalabukhov, A.; Tuzla, N.; Olsson, E.; Claeson, T.; Winkler, D. Nano-patterning of the electron gas at the LaAlO<sub>3</sub>/SrTiO<sub>3</sub> interface using low-energy ion beam irradiation. *Applied Physics Letters* **2013**, *102*.
- [7] D’Antuono, M.; Kalaboukhov, A.; Caruso, R.; Wissberg, S.; Sobelman, S. W.; Kalisky, B.; Auserman, G.; Salluzzo, M.; Stornaiuolo, D. Nanopatterning of oxide 2-dimensional electron systems using low-temperature ion milling. *Nanotechnology* **2021**, *33*, 085301.
- [8] Minhas, M.; Blaschek, H.; Heyroth, F.; Schmidt, G. Sidewall depletion in nano-patterned LAO/STO heterostructures. *Aip Advances* **2016**, *6*.
- [9] Schneider, C. W.; Thiel, S.; Hammerl, G.; Richter, C.; Mannhart, J. Microlithography of electron gases formed at interfaces in oxide heterostructures. *Applied physics letters* **2006**, *89*.
- [10] Bell, C.; Harashima, S.; Kozuka, Y.; Kim, M.; Kim, B. G.; Hikita, Y.; Hwang, H. Dominant mobility modulation by the electric field effect at the LaAlO<sub>3</sub>/SrTiO<sub>3</sub> interface. *Physical review letters* **2009**, *103*, 226802.

- [11] Banerjee, N.; Huijben, M.; Koster, G.; Rijnders, G. Direct patterning of functional interfaces in oxide heterostructures. *Applied Physics Letters* **2012**, *100*.
- [12] Stornaiuolo, D.; Gariglio, S.; Couto, N.; Fête, A.; Caviglia, A.; Seyfarth, G.; Jaccard, D.; Morpurgo, A.; Triscone, J.-M. In-plane electronic confinement in superconducting LaAlO<sub>3</sub>/SrTiO<sub>3</sub> nanostructures. *Applied Physics Letters* **2012**, *101*.
- [13] Gopinadhan, K.; Annadi, A.; Kim, Y.; Srivastava, A.; Kumar, B.; Chen, J.; Coey, J. M. D.; Ariando; Venkatesan, T. Gate Tunable In-and Out-of-Plane Spin–Orbit Coupling and Spin-Splitting Anisotropy at LaAlO<sub>3</sub>/SrTiO<sub>3</sub> (110) Interface. *Advanced Electronic Materials* **2015**, *1*, 1500114.
- [14] Trier, F.; Prawiroatmodjo, G. E.; von Soosten, M.; Christensen, D. V.; Jespersen, T. S.; Chen, Y.; Pryds, N. Patterning of high mobility electron gases at complex oxide interfaces. *Applied Physics Letters* **2015**, *107*.
- [15] Maniv, E.; Ron, A.; Goldstein, M.; Palevski, A.; Dagan, Y. Tunneling into a quantum confinement created by a single-step nanolithography of conducting oxide interfaces. *Physical Review B* **2016**, *94*, 045120.
- [16] Niu, W.; Gan, Y.; Zhang, Y.; Valbjørn Christensen, D.; von Soosten, M.; Wang, X.; Xu, Y.; Zhang, R.; Pryds, N.; Chen, Y. Suppressed carrier density for the patterned high mobility two-dimensional electron gas at  $\gamma$ -Al<sub>2</sub>O<sub>3</sub>/SrTiO<sub>3</sub> heterointerfaces. *Applied Physics Letters* **2017**, *111*.
- [17] Fuchs, D.; Wolff, K.; Schäfer, R.; Thelen, R.; Le Tacon, M.; Schneider, R. Patterning of two-dimensional electron systems in SrTiO<sub>3</sub> based heterostructures using a CeO<sub>2</sub> template. *AIP Advances* **2017**, *7*.
- [18] Bjørlig, A. V.; von Soosten, M.; Erlandsen, R.; Dahm, R. T.; Zhang, Y.; Gan, Y.; Chen, Y.; Pryds, N.; Jespersen, T. S. Nanoscale patterning of electronic devices at the amorphous LaAlO<sub>3</sub>/SrTiO<sub>3</sub> oxide interface using an electron sensitive polymer mask. *Applied Physics Letters* **2018**, *112*.
- [19] Reagor, D. W.; Butko, V. Y. Highly conductive nanolayers on strontium titanate produced by preferential ion-beam etching. *Nature materials* **2005**, *4*, 593–596.
- [20] Harashima, S.; Bell, C.; Kim, M.; Yajima, T.; Hikita, Y.; Hwang, H. Coexistence of two-dimensional and three-dimensional Shubnikov–de Haas oscillations in Ar<sup>+</sup>-irradiated KTaO<sub>3</sub>. *Physical Review B—Condensed Matter and Materials Physics* **2013**, *88*, 085102.
- [21] Bridoux, G.; Barzola-Quiquia, J.; Bern, F.; Böhlmann, W.; Vrejoiu, I.; Ziese, M.; Esquinazi, P. An alternative route towards micro- and nano-patterning of oxide films. *Nanotechnology* **2012**, *23*, 085302.
- [22] Xie, Y.; Hikita, Y.; Bell, C.; Hwang, H. Y. Control of electronic conduction at an oxide heterointerface using surface polar adsorbates. *Nature communications* **2011**, *2*, 494.
- [23] Scheiderer, P.; Pfaff, F.; Gabel, J.; Kamp, M.; Sing, M.; Claessen, R. Surface-interface coupling in an oxide heterostructure: Impact of adsorbates on LaAlO<sub>3</sub>/SrTiO<sub>3</sub>. *Physical Review B* **2015**, *92*, 195422.
- [24] Bristowe, N.; Littlewood, P.; Artacho, E. Surface defects and conduction in polar oxide heterostructures. *Physical Review B—Condensed Matter and Materials Physics* **2011**, *83*, 205405.
- [25] Azimi, S.; Song, J.; Li, C.; Mathew, S.; Breese, M.; Venkatesan, T. Nanoscale lithography of LaAlO<sub>3</sub>/SrTiO<sub>3</sub> wires using silicon stencil masks. *Nanotechnology* **2014**, *25*, 445301.
- [26] Cen, C.; Thiel, S.; Mannhart, J.; Levy, J. Oxide nanoelectronics on demand. *Science* **2009**, *323*, 1026–1030.
- [27] Yu, M.; Liu, C.; Yang, D.; Yan, X.; Du, Q.; Fong, D. D.; Bhattacharya, A.; Irvin, P.; Levy, J. Nanoscale Control of the Metal–Insulator Transition at LaAlO<sub>3</sub>/KTaO<sub>3</sub> Interfaces. *Nano Letters* **2022**, *22*, 6062–6068.

- [28] Cheng, G.; Tomczyk, M.; Lu, S.; Veazey, J. P.; Huang, M.; Irvin, P.; Ryu, S.; Lee, H.; Eom, C.-B.; Hellberg, C. S.; Levy, J. Electron pairing without superconductivity. *Nature* **2015**, *521*, 196–199.
- [29] Cheng, G.; Annadi, A.; Lu, S.; Lee, H.; Lee, J.-W.; Huang, M.; Eom, C.-B.; Irvin, P.; Levy, J. Shubnikov–de Haas–like quantum oscillations in artificial one-dimensional LaAlO<sub>3</sub>/SrTiO<sub>3</sub> electron channels. *Physical review letters* **2018**, *120*, 076801.
- [30] Briggeman, M.; Tomczyk, M.; Tian, B.; Lee, H.; Lee, J.-W.; He, Y.; Tylan-Tyler, A.; Huang, M.; Eom, C.-B.; Pekker, D.; Mong, R. S. K.; Irvin, P.; Levy, J. Pascal conductance series in ballistic one-dimensional LaAlO<sub>3</sub>/SrTiO<sub>3</sub> channels. *Science* **2020**, *367*, 769–772.
- [31] Bi, F.; Bogorin, D. F.; Cen, C.; Bark, C. W.; Park, J.-W.; Eom, C.-B.; Levy, J. “Water-cycle” mechanism for writing and erasing nanostructures at the LaAlO<sub>3</sub>/SrTiO<sub>3</sub> interface. *Applied Physics Letters* **2010**, *97*.
- [32] Liu, Y.; Guo, J.; Zhu, E.; Liao, L.; Lee, S.-J.; Ding, M.; Shakir, I.; Gambin, V.; Huang, Y.; Duan, X. Approaching the Schottky–Mott limit in van der Waals metal–semiconductor junctions. *Nature* **2018**, *557*, 696–700.
- [33] Kong, L.; Zhang, X.; Tao, Q.; Zhang, M.; Dang, W.; Li, Z.; Feng, L.; Liao, L.; Duan, X.; Liu, Y. Doping-free complementary WSe<sub>2</sub> circuit via van der Waals metal integration. *Nature communications* **2020**, *11*, 1866.
- [34] Went, C. M.; Wong, J.; Jahelka, P. R.; Kelzenberg, M.; Biswas, S.; Hunt, M. S.; Carbone, A.; Atwater, H. A. A new metal transfer process for van der Waals contacts to vertical Schottky-junction transition metal dichalcogenide photovoltaics. *Science Advances* **2019**, *5*, eaax6061.
- [35] Chen, Y.; Shu, Z.; Feng, Z.; Kong, L.; Liu, Y.; Duan, H. Reliable Patterning, Transfer Printing and Post-Assembly of Multiscale Adhesion-Free Metallic Structures for Nanogap Device Applications. *Advanced Functional Materials* **2020**, *30*, 2002549.
- [36] Liu, J.; Pang, B.; Xue, R.; Li, R.; Song, J.; Zhao, X.; Wang, D.; Hu, X.; Lu, Y.; Wang, L. Sacrificial layer-assisted nanoscale transfer printing. *Microsystems & Nanoengineering* **2020**, *6*, 80.
- [37] Liu, G.; Tian, Z.; Yang, Z.; Xue, Z.; Zhang, M.; Hu, X.; Wang, Y.; Yang, Y.; Chu, P. K.; Mei, Y.; others Graphene-assisted metal transfer printing for wafer-scale integration of metal electrodes and two-dimensional materials. *Nature Electronics* **2022**, *5*, 275–280.
- [38] Wang, L.; Wang, P.; Huang, J.; Peng, B.; Jia, C.; Qian, Q.; Zhou, J.; Xu, D.; Huang, Y.; Duan, X. A general one-step plug-and-probe approach to top-gated transistors for rapidly probing delicate electronic materials. *Nature Nanotechnology* **2022**, *17*, 1206–1213.
- [39] Yang, X.; Li, J.; Song, R.; Zhao, B.; Tang, J.; Kong, L.; Huang, H.; Zhang, Z.; Liao, L.; Liu, Y.; others Highly reproducible van der Waals integration of two-dimensional electronics on the wafer scale. *Nature Nanotechnology* **2023**, *18*, 471–478.
- [40] Wu, Y.; Xin, Z.; Zhang, Z.; Wang, B.; Peng, R.; Wang, E.; Shi, R.; Liu, Y.; Guo, J.; Liu, K.; others All-Transfer Electrode Interface Engineering Toward Harsh-Environment-Resistant MoS<sub>2</sub> Field-Effect Transistors. *Advanced Materials* **2023**, *35*, 2210735.
- [41] Qi, D.; Li, P.; Ou, H.; Wu, D.; Lian, W.; Wang, Z.; Ouyang, F.; Chai, Y.; Zhang, W. Graphene-Enhanced Metal Transfer Printing for Strong van der Waals Contacts between 3D Metals and 2D Semiconductors. *Advanced Functional Materials* **2023**, *33*, 2301704.
- [42] Zhang, X.; Huang, C.; Li, Z.; Fu, J.; Tian, J.; Ouyang, Z.; Yang, Y.; Shao, X.; Han, Y.; Qiao, Z.; others Reliable wafer-scale integration of two-dimensional materials and metal electrodes with van der Waals contacts. *Nature Communications* **2024**, *15*, 4619.

- [43] He, Y.; Lv, Z.; Liu, Z.; Yang, M.; Ai, W.; Chen, J.; Chen, W.; Wang, B.; Fu, X.; Luo, F.; Wu, J. Sacrifice-layer-free transfer of wafer-scale atomic-layer-deposited dielectrics and full-device stacks for two-dimensional electronics. *Nature Communications* **2025**, *16*, 5904.
- [44] Jeong, J. W.; Yang, S. R.; Hur, Y. H.; Kim, S. W.; Baek, K. M.; Yim, S.; Jang, H.-I.; Park, J. H.; Lee, S. Y.; Park, C.-O.; Jung, Y. S. High-resolution nanotransfer printing applicable to diverse surfaces via interface-targeted adhesion switching. *Nature Communications* **2014**, *5*, 5387.
- [45] Shu, Z.; Feng, B.; Liu, P.; Chen, L.; Liang, H.; Chen, Y.; Yu, J.; Duan, H. Near-zero-adhesion-enabled intact wafer-scale resist-transfer printing for high-fidelity nanofabrication on arbitrary substrates. *International Journal of Extreme Manufacturing* **2023**, *6*, 015102.
- [46] Chen, L.; Liang, H.; Liu, P.; Shu, Z.; Wang, Q.; Dong, X.; Xie, J.; Feng, B.; Duan, H. Phase-Change Stamp with Highly Switchable Adhesion and Stiffness for Damage-Free Multiscale Transfer Printing. *ACS Nano* **2024**, *18*, 23968–23978, PMID: 39177029.
- [47] Niu, R. M.; Liu, G.; Wang, C.; Zhang, G.; Ding, X. D.; Sun, J. Thickness dependent critical strain in submicron Cu films adherent to polymer substrate. *Applied Physics Letters* **2007**, *90*, 161907.
- [48] Lu, N.; Suo, Z.; Vlassak, J. J. The effect of film thickness on the failure strain of polymer-supported metal films. *Acta Materialia* **2010**, *58*, 1679–1687.
- [49] Fan, F.; Chen, L.; Wang, Y.; Wang, P.; Niu, Y.; Lv, Y.; Zhou, Y.; Shu, Z.; Liu, P.; Dong, W.; Zhang, N.; Li, C.; Duan, H. Damage-free dry transfer printing of ultrathin films with on-demand interfacial adhesion: principles and applications. *Soft Science* **2025**, *5*.
- [50] Ha, M. et al. Time reversal symmetry-protected transport at correlated oxide interfaces. *National Science Review* **2025**, *12*, nwaf156.
- [51] Son, J.; Kwon, J.; Kim, S.; Lv, Y.; Yu, J.; Lee, J.-Y.; Ryu, H.; Watanabe, K.; Taniguchi, T.; Garrido-Menacho, R.; Mason, N.; Ertekin, E.; Huang, P. Y.; Lee, G.-H.; van der Zande, A. M. Atomically precise graphene etch stops for three dimensional integrated systems from two dimensional material heterostructures. *Nature Communications* **2018**, *9*, 3988.
- [52] Venkatram, P.; Chen, Z.; Mukhopadhyay, K.; Hengstebeck, B.; Ding, L.; Mazanek, V.; Yang, Y.; Sofer, Z.; Das, S. Two-dimensional crystalline hard masks for high-aspect-ratio nanofabrication. *Nature Materials* **2026**, *25*, 737–746.

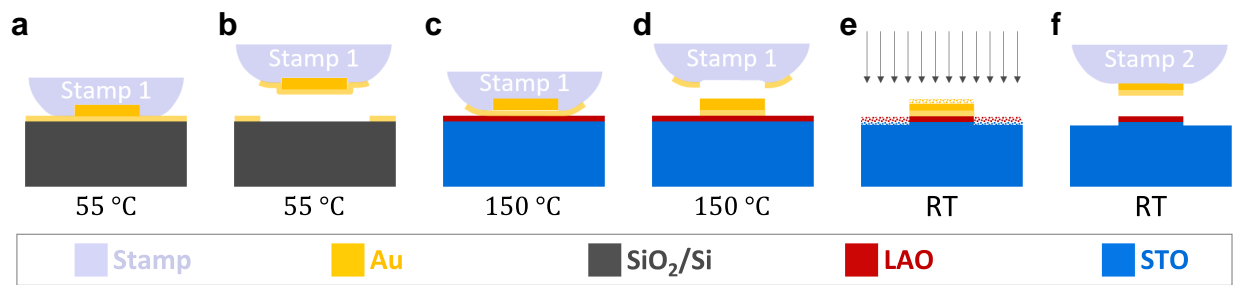


Figure S1: The front-view schematic of the fabrication process in Figure 1. (a,b) A stamp is used to pick up a pre-patterned Au Hall bar mask with a Au isolation layer on SiO<sub>2</sub>/Si. (c,d) The Au Hall bar, along with the thin Au layer directly beneath it, is released on the LAO/STO sample. The Au isolation layer outside the patterned area remains adhered to the stamp, thereby preventing direct contact between the stamp and the sample. (e) Oxygen-enriched Ar<sup>+</sup> ion milling removes the exposed LAO. (f) A second stamp is used to pick up the Au mask on the LAO/STO.

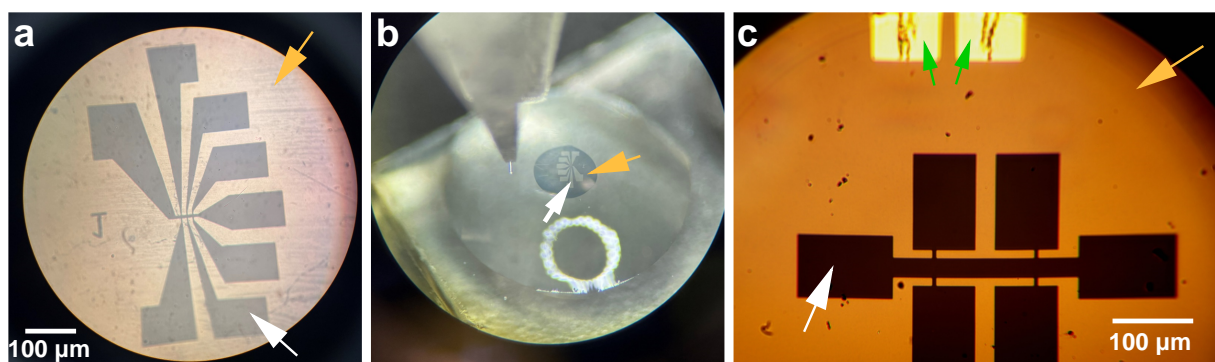


Figure S2: Stamps after the transfer process. The thin Au films outside the patterned areas remain on the stamps (yellow arrows), while the thick Au patterns have been transferred onto target oxide surfaces, exposing the underlying stamp surfaces (white arrows). The green arrows indicate parts of a neighboring thick Au pattern. (a)(b) The stamp shown in Supporting Movie SM2. (c) The stamp shown in Supporting Movie SM3. The particles were introduced accidentally during the process of removing the stamp from the glass slide.

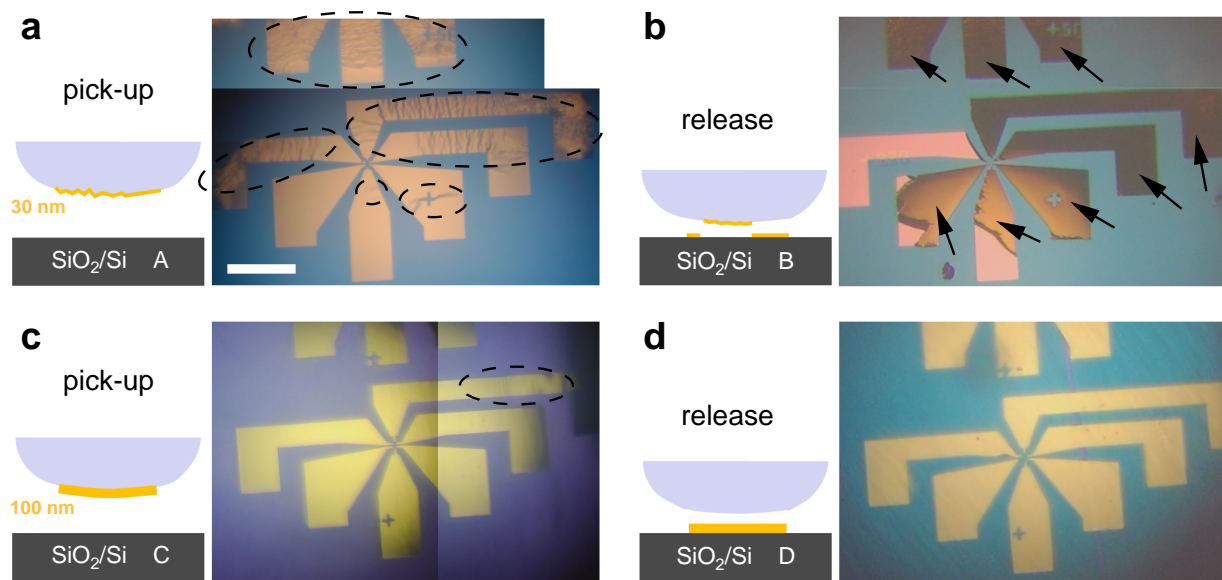


Figure S3: Thickness-dependent Au pattern transfer behavior. Schematic illustrations (left) and corresponding top-view optical micrographs through the stamp (right) are shown for each case. (a) After picking up a 30-nm-thick Au pattern (without the thin Au isolation layer), extensive wrinkles and micro-cracks are observed (black dashed circle). (b) After the release attempt, only portions of the 30-nm-thick pattern are successfully transferred onto SiO<sub>2</sub>/Si. Arrows indicate regions that remain adhered to the stamp. (c) After being picked up, the 100-nm-thick Au pattern (without the isolation layer) remains smooth and crack-free, exhibiting only minor undulations. (d) The entire 100-nm-thick pattern is successfully released onto SiO<sub>2</sub>/Si. Scale bar: 100  $\mu$ m (applies to all optical micrographs). The optical micrographs in panels (a)(b)(c) are composites of two image frames stitched together due to the limited field of view.

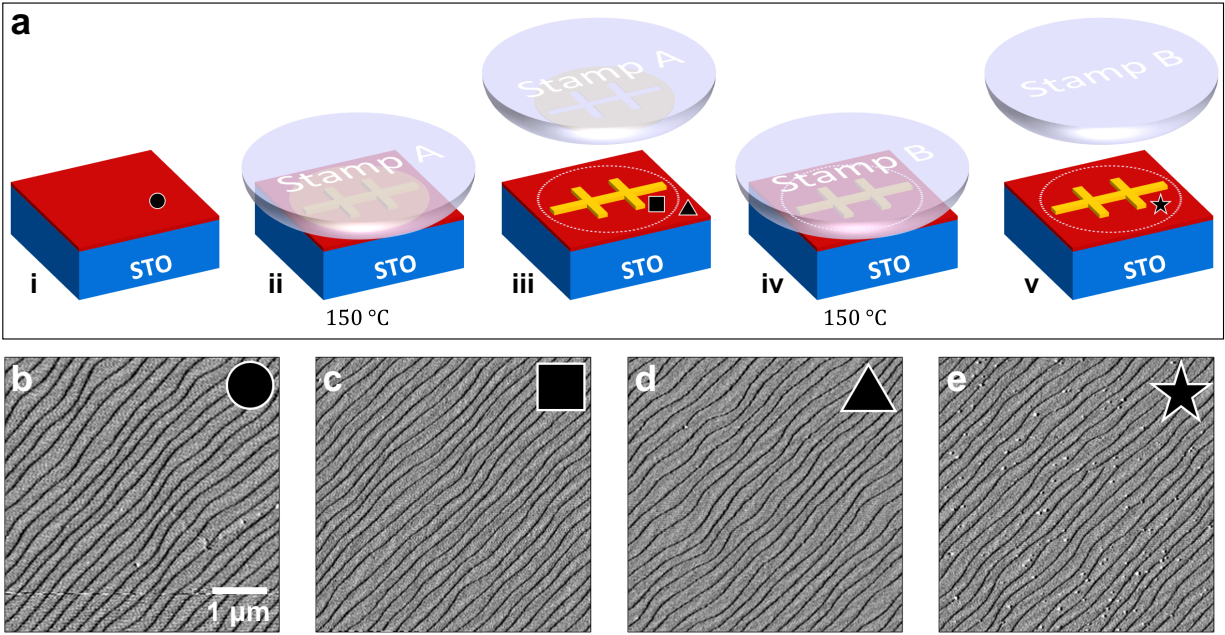


Figure S4: AFM characterization of the oxide surface before and after the Au mask transfer process. (a) Illustration of the treatments on the surface. (b) The original surface was clean before the treatments. (c) The region protected by an Au layer is still clean. (d) The region at the periphery of the stamp's contact area is still clean. (e) The region that was contacted by a stamp at 150 °C shows a few residues with  $\sim 100$  nm diameter and  $\sim 1$  nm height. In contrast, no such contamination is observed in the etched regions that were contacted by a stamp at room temperature, as shown in Figures 2c and 2e.

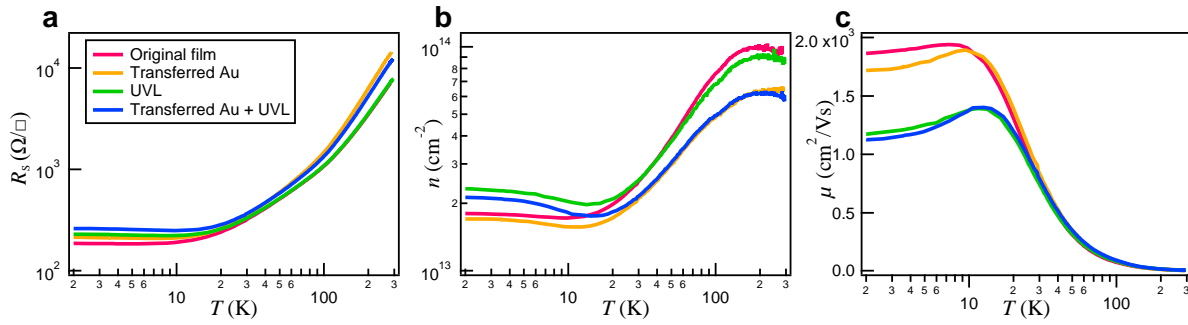


Figure S5: Temperature-dependent transport properties of patterned squares on a low-mobility LAO/STO sample: (a) sheet resistance  $R_s$ , (b) carrier density  $n$ , and (c) mobility  $\mu$  as functions of temperature ( $T = 2\text{--}300\text{ K}$ ) extracted from vdP measurements. The minor mobility difference ( $\sim 8\%$ ) between the original film and the region patterned with the transferred Au mask is attributed to the intrinsic spatial inhomogeneity commonly observed in low-mobility LAO/STO interfaces. This variation is notably smaller than the substantial degradation caused by the UVL process.

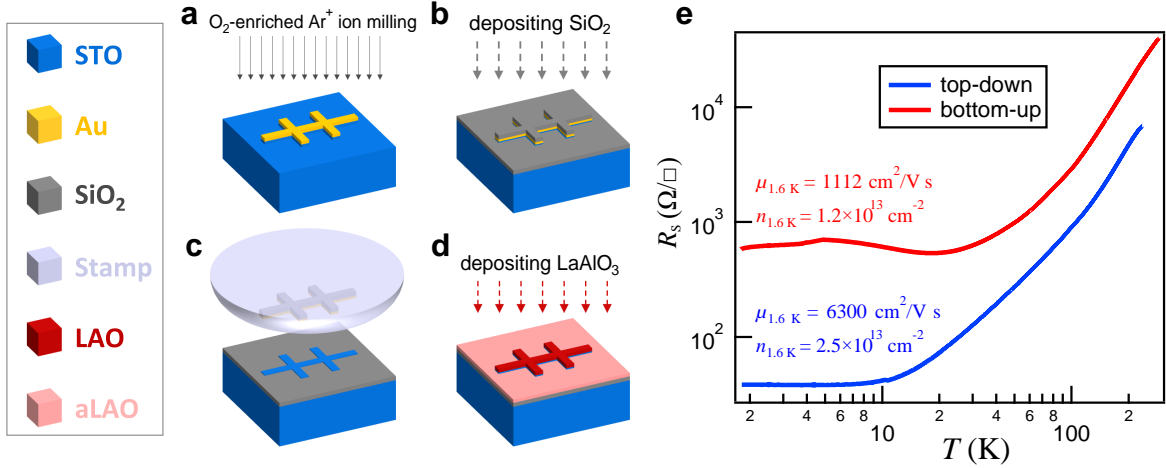


Figure S6: Comparison of the bottom-up and the top-down patterning approaches. (a–d) Illustration of the bottom-up patterning approach: (a) Perform oxygen-enriched Ar<sup>+</sup> ion milling on an STO substrate with a pre-transferred Au Hall bar pattern. (b) Deposit SiO<sub>2</sub> via electron-beam evaporation. (c) Remove the Au pattern along with the overlying SiO<sub>2</sub> using a stamp. (d) Depositing LAO by PLD. The areas outside the Hall bar, being covered by SiO<sub>2</sub>, form amorphous LAO. (e) Comparison of temperature-dependent sheet resistance  $R_s$  of Hall bars patterned by the top-down approach and the bottom-up approach. The LAO deposition parameters (e.g., laser energy, pressure, temperature) are nominally identical. The differences in electronic properties are attributed to the inherent limitation of the bottom-up approach, where the SiO<sub>2</sub> obstructs the substrate area, preventing effective in-situ growth monitoring by reflection high-energy electron diffraction (RHEED) and potentially leading to variations in the interfacial properties compared to the uniformly grown film used in the top-down approach.